Available online at www.sciencedirect.com

ScienceDirect

journal homepage: www.elsevier.com/locate/issn/15375110

Research Paper

Reference trajectory planning under constraints and path tracking using linear time-varying model predictive control for agricultural machines

Mogens M. Graf Plessen[*], *Alberto Bemporad*

IMT School for Advanced Studies Lucca, Piazza S. Francesco, 19-55100 Lucca, Italy

ARTICLE INFO

Article history:
Received 13 June 2016
Received in revised form
18 October 2016
Accepted 26 October 2016
Published online 17 November 2016

Keywords:
Autonomous navigation
Reference trajectory planning
Linear time-varying model
predictive control

A method for the control of autonomously and slowly moving agricultural machinery is presented. Special emphasis is on offline reference trajectory generation tailored for high-precision closed-loop tracking within agricultural fields using linear time-varying model predictive control. When optimisation is carried out, high-level logistical processing can result in edgy reference paths for field coverage. Subsequent trajectory smoothing can consider specific actuator rate constraints and field geometry. The latter step is the subject of this paper. Focussing on forward motion only, the role of non-convexly shaped field geometry, repressed area minimisation and spraying gap avoidance is analysed. Three design methods for generating smooth reference trajectories are discussed: circle-segments, generalised elementary paths, and bi-elementary paths.

1. Introduction

The agricultural sector is experiencing an increasing degree of automation in both the operation of agricultural machinery as well as farm management, Sørensen et al. (2010). This is enabled by the advent of modern computational, sensing and actuating capabilities that allow the implementation of advanced control algorithms. Within this larger context, this paper relates to efficient in-field navigation of agricultural machinery, particularly, to autonomous tractor operation (*auto-steering*).

1.1. *Literature review*

For *reference path generation*, the traditional Dubins Curves method, Dubins (1957), concatenates line segments with circular arcs of minimal admissible turning radius (maximum curvature) to generate shortest pathlength trajectories, focussing on forward motion only. This work was extended in Reeds and Shepp (1990) to also allow for backward motion, while still employing arc and straight segments. Continuous curvature (CC) path planning was then introduced by Fraichard and Scheuer (2004), now adding clothoid arcs as path segments, which in contrast to Dubins Curves, renders the overall path of not minimum length. Within an agricultural context, Backman, Oksanen, and Visala (2012b), Sabelhaus, Röben, zu Helligen, and Lammers (2013) and Backman, Piirainen, and Oksanen (2015) adopted CC path planning using clothoid arcs. The motivation is to take maximum steering rate into account to meet physical actuator constraints. While Sabelhaus et al. (2013) and

* Corresponding author.
E-mail addresses: mogens.plessen@imtlucca.it (M.M. Graf Plessen), alberto.bemporad@imtlucca.it (A. Bemporad).
http://dx.doi.org/10.1016/j.biosystemseng.2016.10.019
1537-5110/

Nomenclature

CC	Continuous curvature path planning
CoR/CoG	Centre of Rotation/Gravitation
HIOP	Headland-interval orthogonal projection
SGA	Spraying gap avoidance
U/Omega-turn	180°-turn in form of an U/Omega
(x,y,ψ)	Vehicle CoG coordinates and heading
(v,δ)	Vehicle velocity, front-axis steering angle
s	Path coordinate
R,l	Turning circle radius, wheelbase
λ	Arc fraction length

Backman et al. (2015) focussed on generating the CC paths for different turning types and allowing forward as well as backward motion, Backman et al. (2012b) implemented CC path planning in an experimental guidance system. However, they did not report quantitative closed-loop tracking errors. Thus, on the analytical level, there exists a trade-off between reference paths of shortest length and continuous curvature.

A nonlinear model predictive control (NMPC) method for a tractor system with towed implement was presented by Backman, Oksanen, and Visala (2012a). It used huge quadratic programming (HQP), Franke (1998), for the solution of its constrained nonlinear optimisation problem by the application of sequential quadratic programming (SQP). Other NMPC control strategies applied in an agricultural autonomous navigation context use the Automatic Control and Dynamic Optimization (ACADO) toolkit, Houska, Ferreau, and Diehl (2011), for the solution of their constrained nonlinear optimisation problems (Kraus et al., 2013; Kayacan, Kayacan, Ramon, & Saeys, 2015a). In Kayacan, Kayacan, Ramon, and Saeys (2015b), a linear time-invariant model predictive control (LTI-MPC) method was employed to minimise the error between a reference yaw rate and the measured yaw rate, and to find a desired steering angle. The longitudinal speed was then controlled by a proportional-integral-derivative (PID) action and an inverse kinematic controller was used for the trajectory tracking. An alternative method reported in an agricultural context is the control of chained systems, Thuilot, Cariou, Martinet, and Berducat (2002). Various closed-loop tracking accuracies have been reported based on real-world experiments. In real-world experiments, reference trajectories have frequently been generated by a human operator manually driving a specific path (e.g., Backman et al., 2012a; Lenain, Thuilot, Cariou, & Martinet, 2006). Tracking errors are usually attributed to noise or similar perturbances (e.g., wheel slip) and counter measures such as state and parameter estimators have therefore been developed.

Considering actuator rate constraints, field geometry for repressed area minimisation and spraying gap avoidance, there exists a research gap with respect to the optimal reference path generation scheme when employed in combination with a control system of interest. Conducting analysis under *nominal* conditions enables additional real-world tracking errors incurred in the field to be attributed to measurement noise and external disturbances.

1.2. *Motivation and contribution*

For reference trajectory tracking within an agricultural context, a linear time-varying model predictive control (LTV-MPC) is considered. It appears suitable in view of accurate vehicle state measurements, differential nonlinear system dynamics, the availability of efficient quadratic programming (QP) solvers, and particularly its ability to account for actuator constraints (such as maximum steering rate constraints). In this paper, the relationship between LTV-MPC and different reference trajectory generation schemes is analysed, with and without analytically continuous curvature. Therefore, the focus is entirely on nominal conditions (noise-free and full state-feedback). Concatenating a straight line with a circle-segment generates a discontinuity in curvature, but is this of practical relevance in a LTV-MPC setting. The questions posed are: How large is the discontinuity? What tracking accuracies are achievable under nominal conditions? What role do steering rate constraints, repressed area minimisation, automatic section control and spraying gap avoidance play when employing different reference trajectories? How much does interpolation of trajectories that occurs naturally within the discrete-time LTV-MPC framework affect results?

These questions are addressed below. The starting point is an edgy path plan for field coverage that was obtained from an in-field logistical optimisation step similar to that obtained by Bochtis and Vougioukas (2008), see Fig. 2. Throughout this paper the focus is to develop methods applicable to arbitrarily non-convex field contours focussing on forward motion of the agricultural machinery. Thus, the perimetric tractor lane (translated in parallel to the field contour) is assumed to be fixed. Thus, all that can be modified is the reference transition trajectories between perimetric and interior tractor lanes.

2. System modelling

2.1. *Kinematics*

Since in-field agricultural machinery operation is typically conducted at low velocity, a motion description purely based on geometric considerations is reasonable. Therefore, a

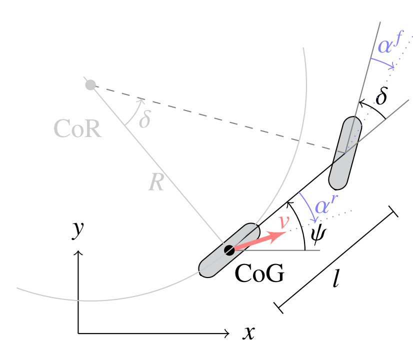

Fig. 1 – The nonlinear kinematic bicycle model (Eq. (2)). The centre of gravity (CoG) is assumed to be located at the centre of the tractor's rear axis. For model (Eq. (1)), or $\alpha^f = \alpha^r = 0$, the instantaneous centre of rotation is indicated by CoR with turning radius R.

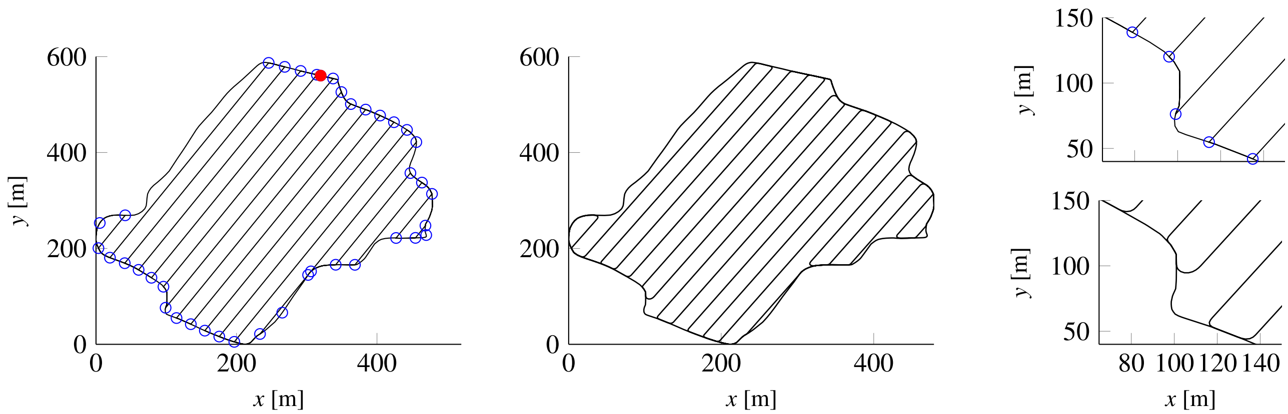

(a) Start constellation (b) Desired: smoothed path (c) Close-ups

Fig. 2 – An illustrative real-world field. (a) Starting constellation: edgy tractor lanes, nodes (blue circles) and entry/exit of field (red dot). An edgy path plan for field coverage is described as a sequence of node visits that is obtained from an in-field logistical optimisation step (not study of this paper). (b) A *smoothed* reference trajectory tailored for high-precision tracking by an autonomous tractor-system (subject of this paper). (c) Close-ups for detailed visualisation.

kinematic bicycle model can be considered, Rajamani (2011), see Fig. 1. It is

$$\begin{bmatrix} \dot{x} \\ \dot{y} \\ \dot{\psi} \end{bmatrix} = \begin{bmatrix} v\cos(\psi) \\ v\sin(\psi) \\ \frac{v}{l}\tan(\delta) \end{bmatrix}, \tag{1}$$

where x and y denote the centre of gravity (CoG) position, assumed to be located at the tractor's rear axis, in the inertial coordinate frame. The yaw angle relative to the inertial coordinates is indicated by ψ. The velocity along the vehicle axle is described by v. The steering input at the front wheels is δ. We refer to l as the wheelbase. An extension of Eq. (1) additionally takes sliding into account, see Lenain, Thuilot, Cariou, and Martinet (2005), resulting in

$$\begin{bmatrix} \dot{x} \\ \dot{y} \\ \dot{\psi} \end{bmatrix} = \begin{bmatrix} v\cos(\psi+\alpha^r) \\ v\sin(\psi+\alpha^r) \\ \frac{v\cos(\alpha^r)}{l}\left(\tan(\delta+\alpha^f)-\tan(\alpha^r)\right) \end{bmatrix}, \tag{2}$$

with sliding parameters α^f and α^r at front and rear wheels.

When employing Eqs. (1) or (2), the tractor and tool are modelled as a unique rigid body as in Thuilot et al. (2002). In contrast, towed implements or trailers may add to the system description. Importantly, under the assumption of no sideways sliding of the trailer, the tractor-trailer relation can be described solely introducing dynamics of the angle between trailer and tractor, Backman et al. (2012a). There is not a single standard description of these dynamics. Multiple approaches exist, dependent on the mechanical design, for example, a passive trailer, a towed implement with articulated joint in the drawbar or a trailer with steering wheels. Oksanen, Timo, and Backman (2015) provided an overview of systems and further details for the equations of motions for multiple different tractor-trailer systems are in Backman, Oksanen, and Visala (2013, 2012a), Oksanen and Visala (2004) and Leng and Minor (2010). In all cases, steering and velocity input reference trajectories are required.

2.2. *Modelling in the time- and space-domain*

A *time-domain* system model description as given in Eqs. (1) and (2) is standard. A second popular choice is its equivalent representation in a *curvilinear* or *road-aligned* coordinate frame as given in Thuilot et al. (2002) and Lenain et al. (2005, 2006). A third method eliminates the time-dependency completely and replaces it with a spatial-based model representation as in Gao et al. (2012) and Graf Plessen, Bernardini, Esen, and Bemporad (2016) for autonomous passenger vehicle operation. In agricultural applications, the main advantage of system descriptions in a curvilinear coordinate system is that the reference with respect to path centreline is constantly zero for path tracking. In contrast, favourable properties of a tractor model using Eq. (1) are the ability to directly work with position coordinates x and y (avoiding any transformations) and avoiding singularities at $v = 0$ when employing more complex and dynamic system models, Graf Plessen et al. (2016).

3. Reference trajectory generation under constraints

3.1. *Problem formulation*

Assuming an in-field logistical optimisation or heuristic step has determined an (edgy) field coverage path, see Fig. 2(a). Then, the objective of this section is to *smooth* this path under consideration of various constraints such that the resulting reference trajectory admits high-precision tracking by an autonomous ground vehicle, see Fig. 2(b).

3.2. *Three design trajectories for path smoothing*

Circle-segments, *generalised elementary paths* and *bi-elementary paths* are considered as design elements for path smoothing.

A *circle* trajectory is characterized by having an instantaneous centre of rotation (CoR) and constant curvature C, i.e., $C(s) = 1/R$, where R is the circle radius and $s \in [0,L]$ with L the path length of the circle-segment.

Next, a *generalised elementary path* is presented as a tool for our application. The work of Funke and Gerdes (2016) which uses two concatenated generalised elementary paths for emergency lane change trajectories when operating autonomous passenger vehicles at their friction limits is summarised. The theoretical basis was developed by Kanayama and Hartman (1997) and Scheuer and Fraichard (1996). Let there be two coordinates $P_i = [x_i,y_i]^T, i = 1,2$, which we wish to connect. We arbitrarily select the initial heading direction of P_1 as $\psi_1 = 0$, see Fig. 3(a). By translation and rotation any other orientation can be achieved. Parameter $\lambda \in [0,1)$ determines the arc fraction length, see Fig. 3(a). A circle-segment is described by $\lambda \rightarrow 1$. A purely clothoid-based trajectory is implied by $\lambda = 0$. For $0 < \lambda < 1$, a generalised elementary path consists of entry clothoid, arc and exit clothoid. Equations describing positions, $x(s)$ and $y(s)$, and heading, $\psi(s)$, along path coordinate $s \in [0,L]$ are derived as

$$d = \sqrt{(x_2 - x_1)^2 + (y_2 - y_1)^2}, \tag{3a}$$

$$\alpha = \psi_2 - \psi_1 = 2 \tan^{-1}\left(\frac{y_2 - y_1}{x_2 - x_1}\right), \tag{3b}$$

$$\begin{aligned} D = {} & 2\int_0^{\frac{\lambda}{2}} \cos\left(\frac{2\alpha}{1+\lambda} z\right) dz + \ldots, \\ & + 2\int_{\frac{\lambda}{2}}^{\frac{1}{2}} \cos\left(\frac{2\alpha}{1-\lambda^2}\left(-z^2 + z - \frac{\lambda^2}{4}\right) z\right) dz, \end{aligned} \tag{3c}$$

$$L = \frac{d}{D}, \quad \sigma = \frac{4\alpha}{L^2(1-\lambda^2)}, \tag{3d}$$

$$\psi(s) = \begin{cases} \psi_1(s) = \int_0^s \sigma z dz, \; s \in \left[0, L\frac{1-\lambda}{2}\right] \\ \psi_2(s) = \int_{L\frac{1-\lambda}{2}}^s \sigma L \frac{1-\lambda}{2} dz + \psi_1\left(L\frac{1-\lambda}{z}\right), s \in \left(L\frac{1-\lambda}{2}, L\frac{1+\lambda}{2}\right) \\ \psi_3(s) = \int_{L\frac{1+\lambda}{2}}^s \sigma(L-z) dz + \psi_2\left(L\frac{1+\lambda}{2}\right), s \in \left[L\frac{1+\lambda}{2}, L\right] \end{cases} \tag{3e}$$

$$x(s) = \int_0^s \cos(\psi(z)) dz + x_1, \; s \in [0, L], \tag{3f}$$

$$y(s) = \int_0^s \sin(\psi(z)) dz + y_1, \; s \in [0, L]. \tag{3g}$$

Analytical solutions to (3d) and part of (3f) do not exist. Therefore, a simple *midpoint rule* for numerical integration is employed.

Our third design trajectory is a *bi-elementary path*. It is a concatenation of two generalised elementary paths, see Fig. 4(a). A characteristic for our application is the identical heading directions at points P_1 and P_3. A bi-elementary path to connect P_1 and P_3 is produced. Given a user-choice parameter γ ("symmetric point fraction"), we compute intermediate location $P_2 = [x_2,y_2]^T$ from Kanayama and Hartman (1997) via $y_2 = (y_3 - y_1)/(x_3 - x_1)x_2 + y_1$, and $\gamma = \left(\sqrt{(x_2 - x_1)^2 + (y_2 - y_1)^2}\right) / \left(\sqrt{(x_3 - x_1)^2 + (y_3 - y_1)^2}\right)$. Let us distinguish first and second elementary paths by superscript ^{1st} and ^{2nd}, and path coordinates $s^{1st} \in [0, L^{1st}]$ and $s^{2nd} \in [0, L^{2nd}]$. Then, we have $\psi^{2nd}(0) = \psi^{1st}(L^{1st})$. With $\alpha^{2nd} = -\alpha^{1st}$, the second elementary path can now be determined following Eq. (3).

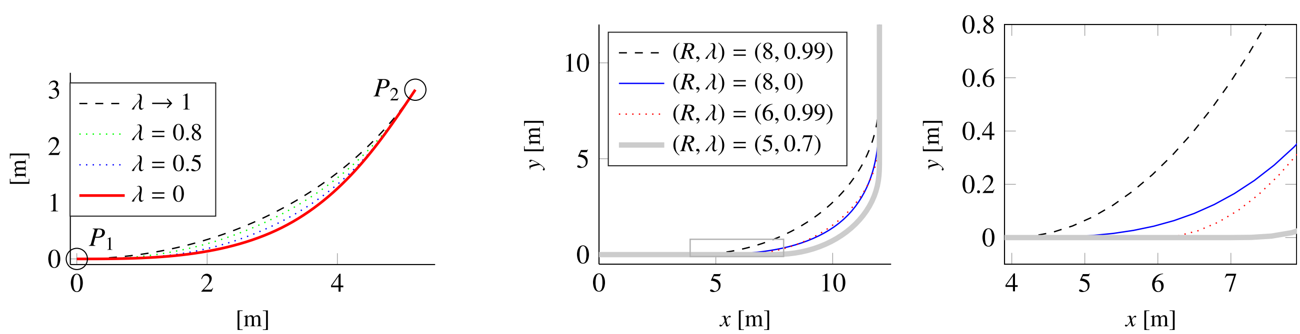

(a) Generalised elementary path. (b) 90°-transition. (c) Close-up.

Fig. 3 – (a) Influence of $\lambda \in [0,1]$ on the shape of a *generalised elementary path*. A circle-segment is given by $\lambda \rightarrow 1$. (b) A 90°-transition for four different parameter selections. The traversal speed is $\bar{v}^{ref} = 10$ km/h. The corresponding steering references are visualised in Fig. 5. (c) Close-up for detailed visualisation. The close-up emphasises the influence of parameter selections on the repressed area, see Table 1. While the case $(R,\lambda) = (6,0.99)$ exceeds $y = 0$ only beyond the $x = 6$ m-mark, the clothoid-based design $(R,\lambda) = (8,0)$ does so before the 5 m-mark.

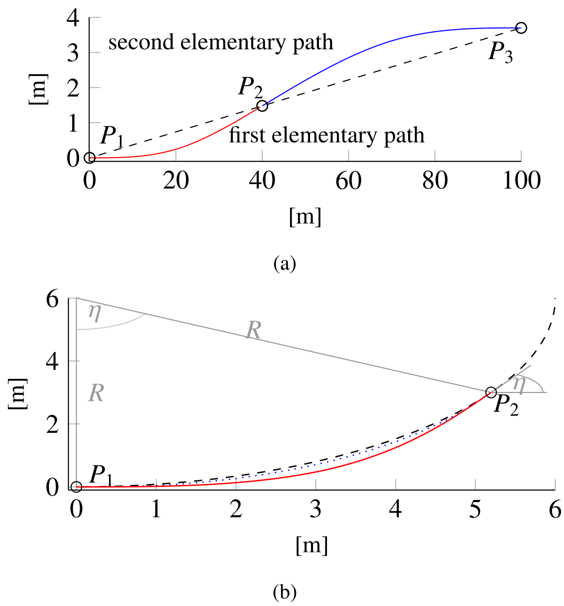

Fig. 4 – (a) Example of a bi-elementary path with $\gamma = 0.4$. For both of the elementary paths we have $\lambda = 0$, respectively. (b) Replacing circle-segments by generalised elementary paths. The black dashed line indicates a quarter circle-segment. Two generalised elementary paths with $\lambda = 0.8$ and $\lambda = 0$ are given by the dotted blue and solid red line, respectively.

To summarise, it remains to select the two points to be connected, to choose one of the three design trajectories therefore, to select parameter λ, and potentially γ.

3.3. *Replacing circle-segments*

A valid question is whether a circle-segment can replace connecting two points, P_1 and P_2, with a generalised elementary path while maintaining the same heading directions at both P_1 and P_2. Without loss of generality, let us set P_1 at the origin with heading $\psi_1 = 0$. Then, it holds Remark 1 below.

Remark 1. A circle segment connecting $P_1 = [0,0]^T$ with $\psi_1 = 0$ and $P_2 = [x_2,y_2]^T$ with $\psi_2 = \eta$, $x_2 > 0$, $y_2 > 0$ can always be replaced by a generalised elementary path, thereby maintaining the same heading directions at P_2.

Proof. The tangent angle to the circle-segment is equal to the angle defining the circle segment (see Fig. 4(b) for visualisation). Thus, $x_2 = R\sin(\eta)$ and $y_2 = R(1-\cos(\eta))$. Under the assumption of $\psi_1 = 0$, we obtain from Eq. (3b) for the generalised elementary path: $\psi_2 = 2\tan^{-1}\left(\frac{y_2-y_1}{x_2-x_1}\right) = 2\tan^{-1}\left(\frac{1-\cos(\eta)}{\sin(\eta)}\right)$. By the trigonometric *tangent half-angle formula* then $\psi_2 = \eta$.

3.4. *Influence of system constraints*

Next, the influence of system constraints on a smooth path trajectory is discussed; considering l, δ_{max}, $\dot{\delta}_{max}$, T_s, $\overline{v}_{ref}$ and the selection of one of the design trajectories. The maximum steering angle and rate of the vehicle are δ^{max} [°] and $\dot{\delta}^{max}$ [°/s]. The control system sampling time is T_s [s]. Trajectories (curves) are traversed at constant speed $\overline{v}_{ref}$ [m/s]. In view of Section 3.3, the main objective is to describe means for determining lower bounds on turning radius R.

Considering the nominal model, Eq. (1), let time index $k \in \mathbb{Z}_+$ be associated with sampling time T_s such that all times of interest can be described as kT_s. Assuming constant input signals, we obtain by integration $\psi_{k+1} = \frac{\overline{v}^{ref}T_s}{l}\tan(\delta_k) + \psi_k$, with the abbreviation $\psi_k = \psi(kT_s)$. The constraints of interest are $|\delta_k| \le \delta^{max}$ and $|\delta_{k+1} - \delta_k| \le \dot{\delta}^{max}T_s$, $\forall t \in [k_1T_s, k_2T_s]$, whereby k_1 and k_2 define the time interval for curve traversal. Thus,

$$\delta_k = \tan^{-1}\left((\psi_{k+1} - \psi_k)\frac{l}{\overline{v}^{ref}T_s}\right), \tag{4}$$

with $k \in [k_1,k_2]$.

Firstly, focussing on circle trajectories. With $s_{k+1} = s_k + T_s\overline{v}^{ref}$ and Eq. (4), $\psi_{k+1} = \int_{s_k}^{s_{k+1}} \frac{1}{R}dz + \psi_k = \frac{1}{R}(s_{k+1} - s_k) + \psi_k$, and consequently $\delta_k = \tan^{-1}\left(\frac{l}{R}\right)$. Transitioning from a straight with $\delta_{k_1-1} = 0$ to a curve at time k_1T_s (and analogously from a curve to a straight at time k_2T_s), and in view of the two aforementioned constraints on δ_k, theoretical lower bounds on the turning radius are obtained as $R(k) = l/\tan(\delta^{max})$, for $k \in \{k_1, \ldots, k_2 - 1\}$, and $R(k) = l/\tan(\dot{\delta}^{max}T_s)$, for $k \in \{k_1 - 1, k_2\}$. For $l = 3$ m, $\delta^{max} = 35°$, $T_s = 0.1$ s and $\dot{\delta}^{max} = 25°/s$, we have $R(k_1-1) = 68.7$ m and $R(k_1) = 4.3$ m. Since the former bound is reached at only two sampling instances, it is typically neglected in practice. Nevertheless, its influence on achievable tracking errors in closed-loop is not obvious.

Analogously, and following Eqs. (3f) and (4), a clothoid-segment can be defined

$$\delta_k = \tan^{-1}\left(\left(s_k + \frac{T_s\overline{v}^{ref}}{2}\right)\sigma l\right), \tag{5}$$

with $k \in K = \{k : s_k \text{ is element of a clothoid path} - \text{segment}\}$ and σ computed from Eqs. (3a)–(3e). Note that in contrast to the circle-case, the argument of $\tan^{-1}(\cdot)$ in Eq. (5) is now linearly dependent on the covered path s_k.

For Eq. (5), because of the missing analytical solution to Eq. (3d), an analytical correspondence to $R(k)$ cannot be computed as for the circle-case. Therefore, we turn to simulations and discuss the case of a 90°-turn. Comparing four different combinations of (R,λ): two circles of different radii, one clothoid-segment ($\lambda = 0$) and one generalised elementary path ($(R,\lambda) = (5,0.7)$) designed such that the rate constraint becomes active. The selections are displayed in Figs. 3 and 5. Several observations can be made. For the purely clothoid-based trajectory, the δ^{max}-constraint becomes active at a much higher radius $R = 8$ than the analytically computed $R_{min}^{circ} = 4.3$ m for the circle-based design. Although the planar trajectories for a circle-based path with $(R,\lambda) = (6,0.99)$ and a clothoid-based equivalent with $(R,\lambda) = (8,0)$ appear similar in Fig. 3(b) (the reason why $R = 6$ was selected), the corresponding steering references are very different, see Fig. 5. Note that $\lambda = 0$ is the most conservative ($\lambda \to 1$ the most aggressive) generalised elementary path possible with respect to steering rate.

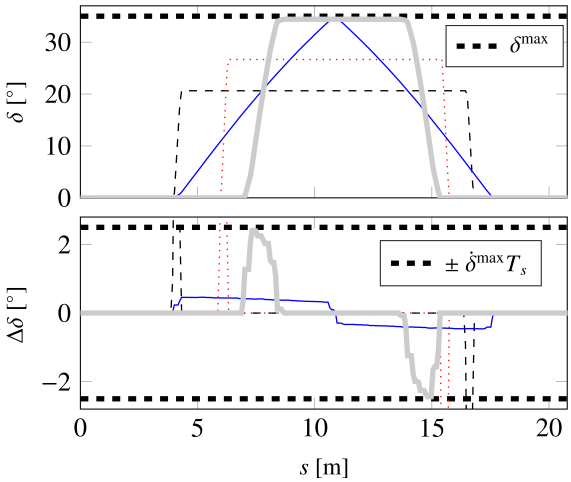

Fig. 5 – The steering references Eq. (4) and their incremental differences for the planar trajectories in Fig. 3(b).

3.5. *Section control and projections*

Algorithm 1. Path smoothing

1: **Input**: desired R and a field plan as in Fig. 2(a) after a potential application of HIOPs as per section 3.5.
2: Identify nodes (D_c in Fig. 6(a), also see Fig. 2(a)) and points along the perimetric lane with sharp turns.
3: **For** every node:
4: Lay two lines of limited length parallel and with distance R to each of a interior lane- and headland-segment adjacent to D_c, such that these two lines intersect within the interior of the perimetric lane and thereby define the instantaneous CoR (e.g., number 25 in Fig. 6(a)).
5: Find the two orthogonal projection points on both the adjacent lane and headland segment, denoted by D_{prev} and D_{next} in Fig. 6(a).
6: Replace edgy path $D_{\text{prev}} \rightarrow D_c \rightarrow D_{\text{next}}$ with a circle-segment connecting D_{prev} and D_{next}.
7: In case of generalised elementary path fitting, using Remark 1, the circle-segment can be replaced with a generalised elementary path.
8: **End For**
9: **Output**: a smoothed path as in Fig. 2(b).

Readily introduced in industry is automatic section control (ASC). It can decrease spraying-overlap, input usage leading to economic savings and additionally reduce environmental impacts, Sharda, Fulton, McDonald, and Brodbeck (2011). Simplistically, while covering the field, the principle is to attempt to apply fertilisers and pesticides only on areas that are not yet sprayed. Referring to Fig. 7 and assuming the headland area is sprayed first, there exists a transition phase (until half of the machine operating width) which is not relevant for the application of fertilisers and pesticides. However, it is important for *repressed area minimisation*, i.e., the avoidance of crop damage becauses of tractor tyre tracks. This can be considered for path trajectory planning. The aim is to minimise $L_{\text{loss}} = 2l_{\text{repr}}w_t g_{\text{gain}}$, where L_{loss} [\$], l_{repr} [m], w_t [m] and g_{gain} [\$m^{-2}] represent total monetary loss due to area repression by tractor tracks, the total length of repressing tractor tracks, the tyre width, and the normalised gain for a crop, respectively. Results for the trajectories in Fig. 3 are summarised in Table 1. Particularly remarkable is the comparison between $(R,\lambda) = (8,0)$ and $(R,\lambda) = (6,0.99)$, see Fig. 3(c). Note that for the coverage of a field, the number of headland turns is typically twice the number of lanes. For example, the field in Fig. 2(b) with a machine operating width of 24 m has 34 headland turns. This further underlines the importance of trajectory design from this perspective.

The notion of *repressed area minimisation* as well as distinction between headland path and interior lanes motivated us to analyse to which is referred to as *headland-interval orthogonal projections* (HIOPs). The concept is explained in Fig. 8. Note that HIOPs are conducted on the edgy path plan for field coverage (Fig. 2(a)) *before* path smoothing. Therefore, two cases must be distinguished: a transition *from* an interior lane towards a headland interval, and the opposite, i.e., a transition from a headland interval *towards* an interior lane. For the former case, the projection point must be located within the interval bounded by the *next* two transition nodes ahead (13 and 12 in Fig. 8 starting from P). For the latter case, the projection point is similarly constrained.

Remark 2. If all headland-to-lane transitions of the initial *edgy* path plan for field coverage are replaced by HIOPs, then angles of at most 90° need to be treated in the subsequent path smoothing step under the assumption that the turning radius, and its equivalent for generalised elementary paths, is at most a quarter of the agricultural headland width H.

Proof. The intersection of an inner application bound (see Fig. 8) and an interior lane is by definition a point, here denoted by P. The orthogonal projection of a point onto an arbitrarily line-segment is by construction the closest point, here denoted by Q, on that line-segment whose tangent is orthogonal to the vector $\overrightarrow{PQ}$. This implies that the length from P to Q is equal to $H/2$. Only in the limit the interior lane may become parallel to both the application bound and headland path at positions P and Q, respectively. In such a case two rectangular corners must be smoothed. By assumption about turning radius and its equivalent for generalised elementary paths (see Remark 1) this is possible. This concludes the proof.

By Remark 2 a bound can be constructed on the required minimal turning radius for a *clothoid-based* generalised elementary path. This was previously not possible since δ_k in Eq. (5) is in general linearly dependent on s_k. Conducting a simulation as illustrated in Fig. 5 for a 90°-turn with variation of parameters until satisfaction of constraints now suffices. An advantage of HIOPs is the *guaranteed* minimisation of repressed area on the *edgy* path level.

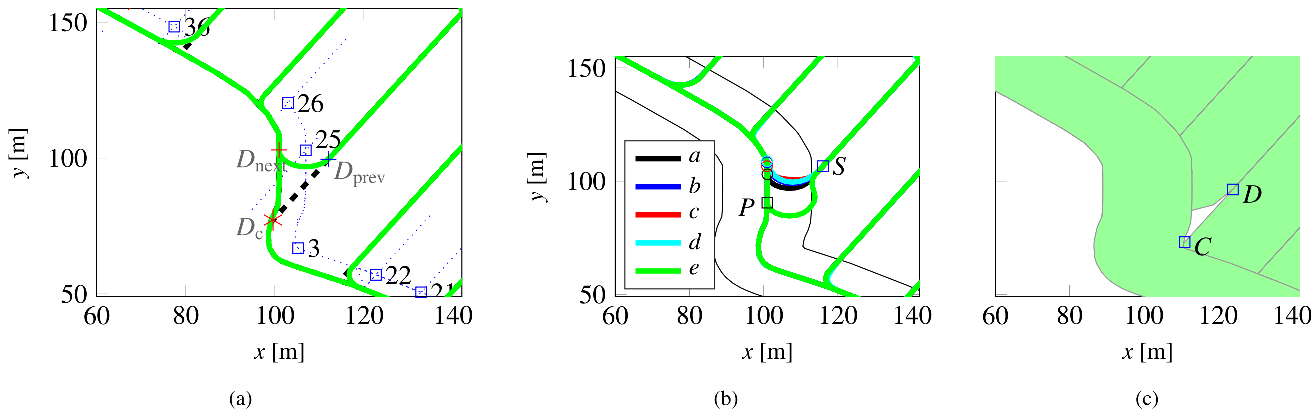

Fig. 6 – (a) Illustration of Algorithm 1 by means of instantaneous centre of rotation (CoR) number 25. (b) Planar reference trajectories for the five cases in Table 2. For the computation of repressed areas, one start point S is set identical to all cases. For each case the pathlength l_{repr} is recorded until next alignment with the perimetric lane indicated by the small circle-markers. For case e, the corresponding point is P. (c) A spraying gap: the white area surrounded by green is geometrically not covered by fertilisers or pesticides when a ground vehicle with operating width W (here equal to headland width H) is following a path as in Fig. 6(a). Two spraying gap corners are denoted by C and D.

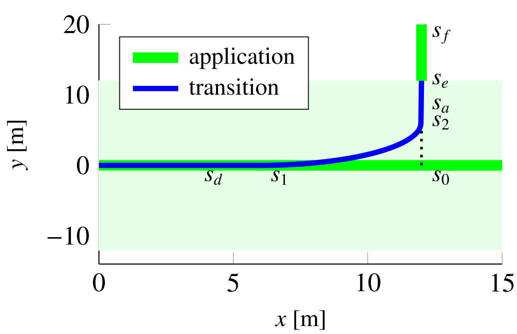

Fig. 7 – The effect of automatic section control on trajectory planning. The horizontal green lane indicates a headland path, while the vertical track ($s_e \rightarrow s_f$) is element of an interior lane beginning at half of the machine operating width (here 12 m). The blue path indicates the transition from headland to lane. In addition, the influence of curve traversal speeds differing from nominal velocity leading to deceleration ($s_d \rightarrow s_1$) and acceleration phases ($s_2 \rightarrow s_a$) is visualised.

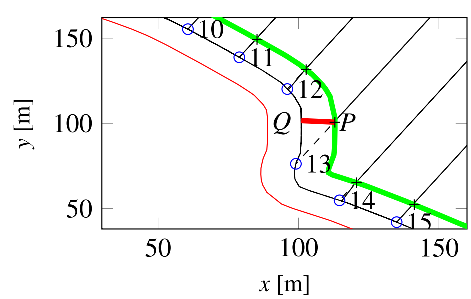

Fig. 8 – Illustration of a headland-interval orthogonal projection (HIOP). The headland area is bounded by the field contour (red) and the inner application bound (green line). The headland width H is the orthogonal distance between red and green line. Instead of traversing from the intersection P of the inner application bound and the field-interior lane to node 13, we determine the projection point Q on the next headland-interval. Thus, the traversal P → 13 → 12 is replaced by P → Q → 12 to minimise the repressed area.

Table 1 – The influence of (R,λ)-combinations on the repressed area defined by $A_{repr} = 2 l_{repr} w_t$, assuming a tyre width of $w_t = 0.75$ m. Pathlength and traversal time, l_{repr} and T_{repr}, are from s_1 to s_e (Fig. 7), $e_{A,m^2} = A_{repr} - \max\{A_{repr}\}$, and $e_{A,\%} = (A_{repr} - \max\{A_{repr}\})/\max\{A_{repr}\}$. Note that the maximum repressed area is obtained for (R,λ) = (8,0).

(R,λ)	T_{repr}	l_{repr}	A_{repr}	e_{A,m^2}	$e_{A,\%}$
(8,0.99)	6.0s	16.8 m	25.2m^2	−1.2m^2	−4.5%
(8,0)	6.3s	17.6 m	26.4m^2	–	–
(6,0.99)	5.7s	15.7 m	23.6m^2	−2.8m^2	−10.6%
(5,0.7)	5.5s	15.3 m	23.0m^2	−3.4m^2	−12.9%

3.6. *Fitting of circles and generalised paths in practice*

The fitting of circles and generalised paths for edge smoothing is illustrated in Fig. 6(a) and Algorithm 1. For increased accuracy in finding a suitable instantaneous CoR, a locally refined grid can be interpolated.

3.7. *Omega-turning*

Before discussing the occurrence of spraying gaps and counter measures to avoid them, *Omega-turns* must be examined. Similar to U-turns, these turns are frequently applied in practice, for example, in the grubbing process.

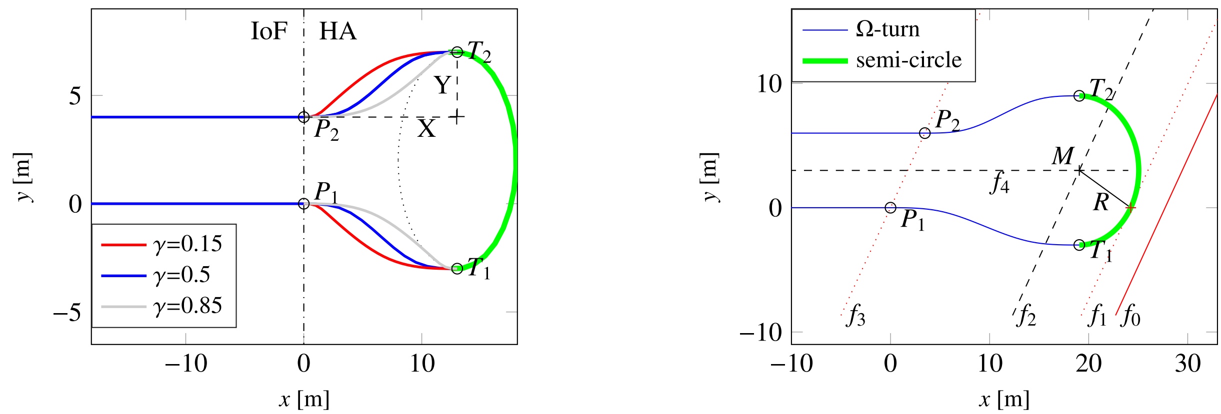

(a) Omega-turn and variation of γ.

(b) Illustration of Algorithm 2.

Fig. 9 – The interior of the field and headland area are denoted by IoF and HA, respectively. Scalars X and Y indicate the absolute length and height of the bi-elementary path. (a) Machine operating width is $W = 4$ to better illustrate the effect of γ. (b) $W = 6$ m, $R = 6$ m and the distance between application bound and field contour (headland width) is $H = 24$ m.

Our preferred method for the construction of an *Omega-turn* is the concatenation of an entry bi-elementary path, a semi-circle and an exit bi-elementary path, see Fig. 9 and Algorithm 2. This combination is suitable because of the identical heading directions at transition points, e.g., T_1 and T_2 in Fig. 9(a). Therefore, however, the centre point M of the circle is constrained to lay symmetrically on a line with heading direction identical to the ones of the intersections between application bound and interior lanes, i.e., points P_1 and P_2 in Fig. 9(b). Bi-elementary paths are composed of two generalised elementary paths, see Section 3.2. Both of them were designed as purely clothoid-based, i.e., with $\lambda = 0$. Varying the symmetric point fraction γ, it was found that best closed-loop tracking results were obtained for $\gamma = 0.5$. It was therefore our preferred choice in all of the following.

Algorithm 2. Omega-turning

1: **Input**: desired R, orthogonal distance H between application bound and field contour, operation width W, field contour f_0, see Fig. 9(b), and two intersections, denoted by P_1 and P_2, between two adjacent interior lanes.
2: Construct two lines, f_1 and f_2, locally parallel to f_0 and with corresponding distances $\frac{W}{2}$ and $\frac{W}{2} + R$.
3: Intersect f_2 with f_4 to determine M.
4: Concatenate a clothoid-based elementary path ($P_1 \rightarrow T_1$), a semicircle ($T_1 \rightarrow T_2$) and a second clothoid-based elementary path ($T_2 \rightarrow P_2$).
5: For pathlength minimisation: while continuously checking constraint satisfaction according to section 3.4, iterate over the location of line f_2 by varying its distance $\frac{W}{2} + R + \epsilon$ from f_0 with $\epsilon > 0$, thereby shifting the location of M.
6: **Output**: An *Omega-turn* connecting P_1 with P_2.

3.8. *Spraying gaps*

Our method for spraying gap avoidance, the SGA-*turn*, is based on bi-elementary paths and circle-segments. It is explained in Fig. 10 and motivated by both geometric and system constraint considerations. With respect to the absolute height of the bi-elementary path segment, see Fig. 9(a), there is an upper bound of *at most* $Y = R$; this is because the circle segment of radius R must be tangent to the perimetric lane. Then, conducting analysis as in Section 3.4, but for an elementary path with $Y = R$ rather than a 90°-turn, a limit can be determined on absolute length X (see Fig. 9(a)) that ensures system constraint satisfaction. Then, for spraying gap avoidance in specific cases, e.g., with $Y < R$, it may reduce X iteratively by ε for reasons of repressed area minimisation (the smaller X, the longer the track stays on a particular interior lane), while continuously checking for constraint satisfaction similarly to Algorithm 2.

Remark 3. For ease of reference, variable names refer to Fig. 10. Under the assumption of straight interior lane trajectories, let all coordinates be transformed by an angle θ via a standard rotation matrix $\tilde{R}(\theta) \in \mathbb{R}^{2\times 2}$, i.e., $[x_\theta, y_\theta]^T = \tilde{R}[x, y]^T$ such that the orientation of all rotated lanes is afterwards aligned with the y_θ-coordinate axis and $y_{\theta,22} \leq y_{\theta,25}$ (to distinguish from the other 180°-orientation). Then, two sufficient conditions for guaranteed avoidance of spraying gaps as indicated in Fig. 6(c) are: $y_{\theta,D} \leq y_{\theta,S}$ and $y_{\theta,22} \leq y_{\theta,C}$.

Proof. By definition, the heading deviation of the CoG of the ground vehicle from lane b starts at position S. Since towed agricultural machinery is oriented perpendicularly to the vehicle heading, the half-distance line is likewise exceeded at level less than $y_{\theta,S}$. By the definition of our concatenation of a bi-elementary path with a circle-segment, the outest tip of the agricultural machinery does not pass the half-distance line again until point C. Thus, the spraying gap left of $x_{\theta,C}$ is now covered. By a similar argument the condition $y_{\theta,22} \leq y_{\theta,C}$ is required to ensure no second spraying gap is created for $x_\theta \geq x_{\theta,C}$, which concludes the proof.

A comparison between five different planar reference trajectories and their influence on both repressed area and spraying gaps is presented in Fig. 6(b) and Table 2. For HIOPs,

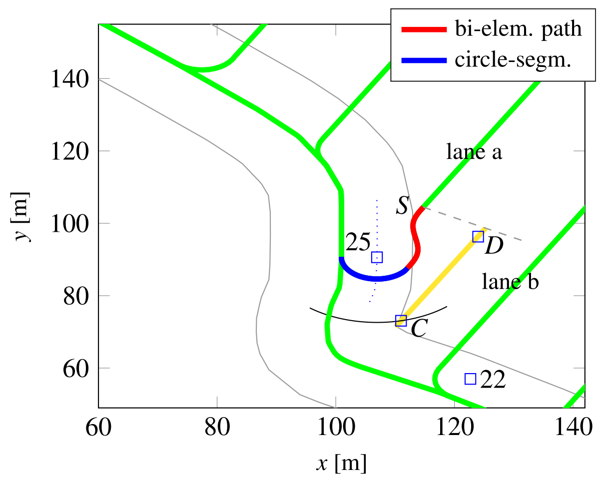

Fig. 10 – Avoidance of spraying gaps. C and D are corners of the spraying gap area (Fig. 6(c)). Start position of the bi-elementary path is indicated by S. The instantaneous centre of rotation for the circle-segment at the end of lane b is denoted by "22". The dotted line-segment denotes points with distance R in parallel to the perimetric (green) lane. The instantaneous centre of rotation "25" for the (blue) circle segment of radius R is found by *sliding* along the dotted line. There are two conditions that must be satisfied for spraying gap avoidance: first, the distance between the instantaneous centre of rotation "25" and point C must be larger or equal R + W/2. The black circle-segment indicates a corresponding curve of radius R + W/2. It intersects at C with the orange line-segment indicating the orthogonal half-distance between lane a and b. Second, the location of the corner D, which is always located along the orthogonal half-distance line, must be below the grey-dashed threshold indicating the start of the turning manoeuvre.

small A_{repr} were expected. When comparing case a and c, this is the case. In contrast, for case b and d not. The reason is that the corresponding distance $|\overrightarrow{PQ}|$ (see Fig. 8) is here already so small such that only one clothoid can be fitted (for $R = 6$ there are two). This explains the larger $A_{repr} = 36.1$ m^2. The comparison of case a with b is in line with the results from Section 3.5. The clothoid-based solution with $R = 8$ causes more repressed area because of an earlier deviation from the lane in contrast to its circle-based counterpart with $R = 6$. The resulting spraying gap is here significantly, by 33%, larger for case b, which is due to the nonlinearly shaped perimetric lane and the corresponding alignment points for case a and b. Ultimately, as expected, case e produces much more repressed area, e.g., 51% or 18 m^2 more than case a, but in contrast avoids the spraying gap. Here, the farm manager must decide the trade-off between repressed area minimisation and spraying gap avoidance.

Table 2 – For visualisation, see Fig. 6(b). $A_{repr} = 2l_{repr}w_t$ and assuming a tyre width of 0.75 m. The spraying gap area is denoted by $A_{spray,miss}$. Case e can avoid the spraying gap. However, it then incurs an additional overlapping area of 111.6 m^2.

Case	(R,λ)	Remark	A_{repr}	$A_{spray,miss}$
a	(6,0.99)	–	35.5 m^2	45.0 m^2
b	(8,0)	–	36.8 m^2	59.8 m^2
c	(6,0.99)	HIOP	31.5 m^2	61.0 m^2
d	(8,0)	HIOP	36.1 m^2	66.1 m^2
e	(6,0.99)	SGA-turn	53.5 m^2	0

3.9. *Reference velocity trajectories*

With respect to models in Eqs. (1) and (2), besides steering angle, a reference trajectory for vehicle speed is required. We decide to traverse the curve at constant speed $\overline{v}^{ref} \le v^{des}$, with v^{des} the desired velocity along straight lanes, and conduct any possible deceleration and acceleration before and after the curve at (absolute) rates $\dot{v}^{min}$ and $\dot{v}^{max}$. This is reasonable in view of expected slippage in a real-world application. For illustration, see Fig. 7. Denoting the start position of the curve along the path by s_1 and the associated time by t_1, the deceleration phase length can be computed as $\Delta t_d = v^{des} - \overline{v}^{ref}/\dot{v}^{min}$ and the corresponding start position s_d as $s_d = -\dot{v}^{min}\Delta t_d^2/2 + v^{des}\Delta t_d + s_1$, and similarly for the acceleration phase with Δt_a and s_a. Knowledge of lane position, R and curve shape enables us to easily determine s_1 and s_2. Vehicle reference trajectories can then be derived as piecewise-affine.

3.10. *A remark to actively-steered trailers*

An actively-steered trailer allows a tractor-trailer operation such that repressed area traces due to the towed implement are better avoided. Tractor and trailer can be steered such that they better follow the same tyre-traces.

Let us consider the tractor-trailer system from Backman et al. (2012b), where the focus was on the application of nonlinear model predictive control for path tracking. The corresponding reference path trajectory was created manually by a human operator generating a curved driving line. By contrast, we here discuss how trailer geometry and constraints can be considered for the design of a minimal turning radius R. Following (Backman et al., 2012b, Fig. 2), we differentiate between two control points, standardly the centre position of the tractor rear axle (CoG), and the centre position of the trailer (position E). Normalising coordinates, the geometric relation between CoG and location E is

$$\begin{bmatrix} x_E \\ y_E \end{bmatrix} = \begin{bmatrix} -b - c\cos(\beta) - d\cos(\beta+\gamma) \\ c\sin(\beta) + d\sin(\beta+\gamma) \end{bmatrix}, \tag{6}$$

where $\gamma \in [-\gamma_{max}, \gamma_{max}]$ denotes the new control variable (besides v and δ), and $\beta \in [-\beta_{max}, \beta_{max}]$ is the angle between trailer and tractor, see Fig. 11.

An auxiliary point T is introduced such that $[x_T, y_T] = [-R\cos(\pi/2 - \beta - \gamma_{max}), R(1 - \sin(\pi/2 - \beta - \gamma_{max}))]$ and $[x_T, y_T] = [-b - c\cos(\beta) - l\cos(\beta + \gamma_{max}), c\sin(\beta) + l\sin(\beta + \gamma_{max})]$. When selecting an arbitrary $\beta \in [-\beta_{max}, \beta_{max}]$, these two equations can be used to find the two variables l and R, and thereby also point T, Fig. 11. The smaller the selected β, the larger R and the closer T to point E. The larger β, the smaller R and the closer T is to C. Dependent on the application, a specific T-location and thus R might be preferable.

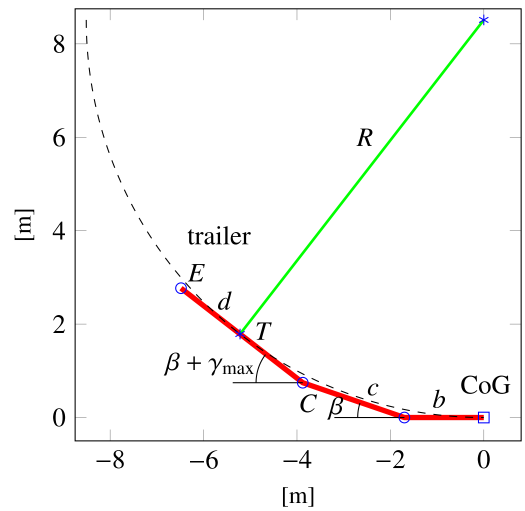

Fig. 11 – Influence of trailer geometry on turning radius. The tractor's CoG is normalised at the origin, while, the trailer's control point is denoted by E. Parameters (from Backman et al. (2012b)) are: $b = 1.7$ m, $c = 2.3$ m, $d = 3.3$, $\gamma_{\max} = 0.33$ rad and $\beta_{\max} = 1.57$ rad. Point T and CoG are elements of a circle-segment with a radius of, here, $R = 8.5$ m for $\beta = \gamma_{\max}$.

4. Reference trajectory tracking

All of Section 3 was concerned about reference trajectory generation. A control method is now presented to track z^{ref} and u^{ref} with states $z = [x, y, \psi]^T \in \mathbb{R}^3$ and controls $u = [v, \delta]^T \in \mathbb{R}^2$. For the autonomous navigation of agricultural machines, we propose to use linear time-varying model predictive control (LTV-MPC). For our agricultural setting a closed-loop feedback control architecture is adopted according to Graf Plessen et al. (2016) as visualised in Fig. 12. Numerical values of system parameters $(l, T_s, \delta^{\max}$, etc.) are chosen as in Section 3.4.

4.1. *Linearisation and discretisation*

Let us consider the system Eq. (2), which includes Eq. (1) by setting $\alpha^r = \alpha^f = 0$, and which can be summarised as $\dot{z} = f(z, u)$ with $z = [x, y, \psi]^T$ and $u = [v, \delta]^T$. The approach is easily extendable when additionally considering towed implement and similar dynamics.

Firstly, Eq. (2) is linearised using a first-order Taylor approximation around the reference trajectories (from Section 3) as

$$\dot{z} \approx f(z^{\text{ref}}, u^{\text{ref}}) + A(z - z^{\text{ref}}) + B(u - u^{\text{ref}}), \tag{7}$$

where $A = \frac{\partial f(z^{\text{ref}}, u^{\text{ref}})}{\partial z}$ and $B = \frac{\partial f(z^{\text{ref}}, u^{\text{ref}})}{\partial u}$ obtaining

$$A = \begin{bmatrix} 0 & 0 & -v^{\text{ref}} \sin(\psi^{\text{ref}} + \alpha^r) \\ 0 & 0 & v^{\text{ref}} \cos(\psi^{\text{ref}} + \alpha^r) \\ 0 & 0 & 0 \end{bmatrix},$$

$$B = \begin{bmatrix} \cos(\psi^{\text{ref}} + \alpha^r) & 0 \\ \sin(\psi^{\text{ref}} + \alpha^r) & 0 \\ \frac{\cos(\alpha^r)}{L}\left(\tan(\delta^{\text{ref}} + \alpha^f) - \tan(\alpha^r)\right) & \frac{v^{\text{ref}} \cos(\alpha^r)}{L\cos^2(\delta^{\text{ref}} + \alpha^f)} \end{bmatrix}. \tag{8}$$

Under the assumption of $u(t) = u_k$, and $k \in \mathbb{N}$ indexing steps over $t \in [kT_s, (k+1)T_s]$ with sampling time T_s, the exact discretisation: $z_{k+1} = z_k e^{AT_s} + \left(\int_0^{T_s} e^{A\eta} d\eta\right)\left(B(u_k - u_k^{\text{ref}}) + f(z_k^{\text{ref}}, u_k^{\text{ref}}) - Az_k^{\text{ref}}\right)$ is obtained. In general, for the evaluation of integrals involving matrix exponentials we refer to Van Loan (1978). In our specific case, Remark 4 holds, which is highly beneficial for an embedded implementation, since it allows a very simple transformation of (7) into a discrete-time model $z_{k+1} = A_k z_k + B_k u_k + g_k$, with $A_k \in \mathbb{R}^{3\times3}$, $B_k \in \mathbb{R}^{3\times2}$ and $g_k \in \mathbb{R}^{3\times1}$.

Remark 4. For the linearised system of Eq. (2) it holds that $\int_0^{T_s} e^{A\eta} d\eta = T_s I + \frac{AT_s^2}{2}$, where I is the identity matrix.

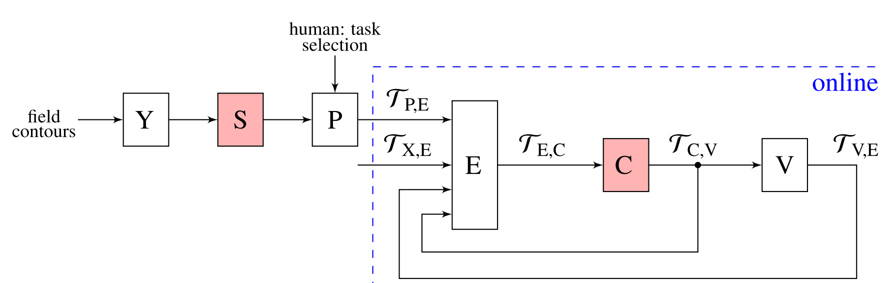

Fig. 12 – Closed-loop feedback control architecture. A human supervisor selects a task such as, e.g., field coverage or tasks as discussed in Graf Plessen and Bemporad (2016), thereby determining path plan P. The remaining symbols are as follows. Y: high-level graph-theoretic logistical optimisation step resulting in *edgy* reference paths for field coverage. S: *smooth* trajectory generation, see Section 3. E: sensor fusion/model-based state estimation. C (controller): online LTV-MPC formulation and QP-solver, see Section 4. V: low-level controllers and nonlinear vehicle dynamics. $T_{P,E}$: path plan. $T_{X,E}$: exteroceptive measurements, i.e., surrounding perception. $T_{V,E}$: proprioceptive measurements. $T_{E,C}$: perception, localization, constraint and reference information. $T_{C,V}$: high-level controls. The topics subject of this paper are emphasised in red.

PROOF. A Taylor series expansion reads $e^{A\eta} = I + A\eta + \frac{A^2\eta^2}{2!} + \ldots + \frac{(A\eta)^k}{k!} + \ldots$. Our A in Eq. (8) is square and nilpotent, i.e., $A^n = 0, \forall n > 1$.

4.2. Linear time-varying model predictive control

We formulate the LTV-MPC problem in form of a QP:

$$\min_{\{u_j\}_{j=0}^{N-1}} \sum_{j=1}^{N-1} \| z_j - z_j^{\mathrm{ref}} \|_{Q_z}^2 + \sum_{j=0}^{N-1} \Big(\| u_j - u_j^{\mathrm{ref}} \|_{Q_u}^2 + \| u_j - u_{j-1} \|_{Q_{\Delta u}}^2 \Big) + \| z_N - z_N^{\mathrm{ref}} \|_{Q_{zN}}^2 \tag{9a}$$

$$\text{s.t.} \quad z_0 = z_k \tag{9b}$$

$$u_{-1} = u_{k-1}^{\star} \tag{9c}$$

$$z_{j+1} = A_j z_j + B_j u_j + g_j, \; j = 0, \ldots, N-1, \tag{9d}$$

$$u^{\min} \le u_j \le u^{\max}, \; j = 0, \ldots, N-1, \tag{9e}$$

$$\Delta u^{\min} \le u_j - u_{j-1} \le \Delta u^{\max}, \; j = 0, \ldots, N-1, \tag{9f}$$

with prediction horizon N. The objective function penalises reference tracking errors and input signal changes. Vector $u_{k-1}^{\star}$ indicates the input applied to the system at the previous sampling time $(k-1)T_s$. The parameters Q_z, Q_u, $Q_{\Delta u}$, Q_{zN} are tuning weights of appropriate dimension, where we use the general notation $\|x\|_Q^2 = x^T Q x$ for $x \in \mathbb{R}^n$ and a positive definite matrix $Q \in \mathbb{S}_{++}^n$. Constant upper and lower bounds are $u^{\min}$, $u^{\max}$, $\Delta u^{\min} = \dot{u}^{\min} T_s$ and $\Delta u^{\max} = \dot{u}^{\max} T_s$, where $\dot{u}^{\min}$ and $\dot{u}^{\max}$ denote the rate constraints.

By elimination of states $\{z_j\}_{j=1}^N$ we transform (9) into QP-form:

$$\min_w \frac{1}{2} w^T Q w + f^T w \tag{10a}$$

$$\text{s.t.} \quad Gw \le g, \tag{10b}$$

where $w = [u_0^T, u_1^T, \ldots, u_{N-1}^T]^T$ and the derivation of Q, f, G and g is achieved by recursive substitution.

Algorithm 3. Alternating direction method of multipliers (ADMM) for the solution of Eq. (10)

1: **Input**: Q, f, G, g, w^0.
2: **Parameters**: $\rho = 1000$, $\epsilon^{\mathrm{abs}} = 10^{-1}$, `maxIter` $= 100$.
3: **Initialisation**: $p^0 = \max\{g - Gw^0, 0\}$, $p^{-1} = p^0$, $q^0 = 0$.
4: **For** $i = 0, \ldots,$ `maxIter`:
5: $\quad w^{i+1} = (Q + \rho G^T G)^{-1} \left(-f - \rho G^T (p^i - g + q^i) \right)$.
6: $\quad p^{i+1} = \max\{g - Gw^{i+1} - q^i, 0\}$.
7: $\quad q^{i+1} = q^i + Gw^{i+1} + p^{i+1} - g$.
8: $\quad r^{i+1} = Gw^{i+1} + p^{i+1} - g$, and $s^{i+1} = \rho G^T (p^{i+1} - p^i)$.
9: $\quad$ If $\|r^{i+1}\|_2 < \epsilon^{\mathrm{abs}}$ and $\|s^{i+1}\|_2 < \epsilon^{\mathrm{abs}}$, break, go to step 11.
10: **End For**
11: **Output**: $w^{\star} = w^{i+1}$.

4.3. QP-solving via alternating direction method of multipliers

An ADMM-solution was implemented (Boyd, Parikh, Chu, Peleato, & Eckstein, 2011, Section 3.1), for Eq. (10). Because of the MPC-setting, we employ a warm-start for optimisation variable w. This accelerated computational speed. Primal and dual residuals are used as a termination criterion. Treating tolerances for primal and dual residuals separately were tested as outlined in Boyd et al. (2011), Section 3.3.1. However, no decrease in computational time could be observed. Likewise, testing a varying penalty parameter (Boyd et al., 2011, Section 3.4.1) did not accelerate processing. The choice of penalty parameter $\rho > 0$ was highly influential. A large ρ emphasises feasibility and constraint satisfaction. Simulation results were compared when employing ADMM and Matlab's `quadprog` as QP-solvers, respectively, and it was found that a large ρ with small stopping tolerance, $\varepsilon^{\mathrm{abs}}$, and small maximum admissible number of ADMM-iterations, `maxIter`, yielded the shortest computation times, while not compromising required solution accuracy. For example, using $\varepsilon^{\mathrm{abs}} = 10^{-3}$ instead of 10^{-1} increased the average computation time from 0.7 ms to 0.9 ms, but did not change the closed-loop tracking accuracy. Frequently, only a single ADMM-iteration was required to find a solution. Dependent on the reference trajectory, however, it also occurred that `maxIter` was reached repeatedly. Emphasising the simplicity, our complete ADMM-algorithm for the solution of Eq. (10) is stated in Algorithm 3. The computational most demanding step is the solution of a least-squares problem (step 5). Since matrix Q in (10) is time-varying, the inverse $(Q + \rho G^T G)^{-1}$ cannot be precomputed offline beforehand, but must be updated at every sampling time T_s.

4.4. QP-solving via Accelerated Dual Gradient Projection scheme

As an alternative to ADMM, we also implemented a Accelerated Dual Gradient Projection scheme (GPAD-solution), see Patrinos and Bemporad (2014), which solves the dual problem of Eq. (10) using an accelerated gradient projection method. Let the corresponding dual variable be denoted by d. A warm-start of d increased computational speed. For ease of reproduction, we state Algorithm 4. Parameters were tuned for speed, nevertheless, still maintaining a sufficient solution accuracy specifically with respect to feasibility. The computation of Lipschitz constant $\mathscr{L}$ was by far the most expensive step. To give a numerical value for our application, typically $\mathscr{L}$ was around 0.0468. Without any preconditioning or dual scaling, for average runtimes of 1.6 ms and 1.3 ms (see Table 3) for the completion of Algorithm 4, a remarkable 1.06 ms was used to find $\mathscr{L}$, which corresponds to 66% and 82%, respectively.

Table 3 – Nominal closed-loop simulation results for the experiment of a 90°-transition, see Section 5.1.

(R,λ)	$\overline{\tau}_{\mathrm{build}}$	$\overline{\tau}_q/\overline{\tau}_g/\overline{\tau}_a$	$\tau_q^{\max}/\tau_g^{\max}/\tau_a^{\max}$	$\max\{e_k^{\mathrm{abs}}\}$
(8,0.99)	2.0	6.3/1.5/0.7	9.0/3.0/2.0	1.2
(8,0)	2.1	6.2/1.3/0.7	8.4/1.9/2.1	0.5
(6,0.99)	2.1	6.1/1.6/0.7	8.6/3.3/2.0	2.1
(5,0.7)	2.0	6.2/1.9/0.7	21.8/4.2/2.0	5.3

4.5. A brief remark to state estimation

Recursive state estimation, sensor fusion, or adaptation of parameters such as, e.g., sliding parameters α^r and α^f in (2), are not subject of this paper. However, it should be noted that in case of moving horizon estimation (MHE), see Kraus et al. (2013), and a corresponding QP, Algorithms 3 and 4 may also be employed. The more common alternative to MHE are extended Kalman filters (EKFs), see Backman et al. (2012a), which rely on only the evaluation of algebraic equations.

Algorithm 4. GPAD for the solution of Eq. (10)

1: **Input**: Q, f, G, g, d^0.
2: **Parameters**: $\epsilon^{\text{feas}} = 10^{-2}$, $\epsilon^{\text{opt}} = 10^{-1}$, $\texttt{maxIter} = 200$.
3: **Initialisation**: $d^{-1} = d^0$, $\mathcal{L} = \|GQ^{-1}G^T\|_2$.
4: **For** $i = 0, \ldots, \texttt{maxIter}$:
5: If $i = 0$: $\beta^i = 0$, else: $\beta^i = (i-1)/(i+2)$.
6: $e^i = d^i + \beta^i(d^i - d^{i-1})$.
7: $w^i = -Q^{-1}(G^T e^i - f)$.
8: $h^i = (Gw^i - g)/\mathcal{L}$.
9: **If** $h^i_j \le \epsilon^{\text{feas}}$, $\forall j$ (i.e., elementwise check):
10: If $-(e^i)^T h^i \le \epsilon^{\text{opt}}/\mathcal{L}$: break, go to step 14.
11: **End If**
12: $d^{i+1} = \max\{e^i + h^i, 0\}$.
13: **End For**
14: **Output**: $w^\star = w^i$, $d^\star = d^i$.

5. Nominal closed-loop simulation experiments

Here the *nominal* accuracy that can be achieved by a combination of above reference trajectory designs and using LTV-MPC for closed-loop reference tracking are analysed. The focus is on LTV-MPC only. In view of the nonlinear path trajectories, a straightforward application of LTI-MPC is not feasible. Implementations of comparative NMPC are computationally significantly more expensive (Falcone, Borrelli, Tseng, Asgari, & Hrovat, 2008), and are therefore omitted from this discussion. Note, however, that interpretations of different reference trajectory designs would nevertheless be identical, i.e., likewise dependent on reference steering rates (not) violating corresponding constraints as discussed below. Note also that low single-digit cm-precision is already obtainable by LTV-MPC as discussed in the following. The control commands are applied to the original nonlinear model Eq. (1). System states are integrated forward using Matlab's `ode23tb`. Assuming noise-free and full state feedback, and additionally comparing computation times of three QP-solvers, throughout this section, MPC weights are set as $Q_z = \text{diag}[1000,1000,1000]$, $Q_{zN} = Q_z$, $Q_u = \text{diag}[100,100]$ and $Q_{\Delta u} = \text{diag}[1,1]$. Different prediction horizon lengths N were tested. For smaller N the tracking accuracy decreases. For too large N the computational cost increases while not yielding smaller tracking errors. For $T_s = 0.1$ s and an average travelling speed of $v = 10$ km/h, $N = 20$ was found to be a good compromise. It implies a prediction horizon of $T_s v(N+1) = 5.8$ m, a total number of $Nn_u = 40$ optimisation variables, and $4Nn_u = 160$ inequality constraints. All simulations were conducted on a laptop running Ubuntu 14.04 equipped with an Intel Core i7 CPU @2.80GHz × 8, 15.6 GB of memory, and using MATLAB 8.6 (R2015b). Reported computation times τ are in milliseconds. Regarding the LTV-MPC problem, $\overline{\tau}_{\text{build}}$ includes linearisation, discretisation and building of the QPs. The average and maximum computation times using MATLAB's `quadprog`, GPAD and ADMM for the solution of the QPs are denoted by $\overline{\tau}_q$, $\tau_q^{\max}$, $\overline{\tau}_g$, $\tau_g^{\max}$, $\overline{\tau}_a$ and $\tau_a^{\max}$, respectively. The solution procedures are made comparable based on an identical tracking error criterion. The absolute tracking error is defined as $e_k^{\text{abs}} = \sqrt{(x_k - x_k^{\text{ref}})^2 + (y_k - y_k^{\text{ref}})^2}$ and were always reported in unit of centimetres.

5.1. A 90-degree turn

For the corresponding reference trajectories, see Fig. 3 and Table 1. Closed-loop results are summarised in Table 3 and Fig. 13. Several observations can be made. For the two circle-based methods ($R \in \{8,6\}$ and $\lambda = 0.99$), the larger the turning radius, the smaller is $\max\{e_k^{\text{abs}}\}$. The QP-ADMM solver outperforms `quadprog` and GPAD on average by factors 9 and 2 with respect to average runtimes. Even more important, ADMM offers consistently lower and quasi constant worst-case runtimes. The smallest nominal maximal tracking error, a remarkable 0.5 cm, can be achieved for the purely clothoid-based solution with $(R,\lambda) = (8,0)$. The reasons is that reference trajectories are here satisfying in particular also steering rate constraints, see Fig. 13(b). In a MPC-setting, it is unavoidable to conduct interpolations such that reference trajectories begin at a given current state. Likewise, concatenating path elements, e.g., the one in Fig. 3 with straights at the beginning and end, also requires interpolating, possibly even to a non-uniform space-grid. Given reference position coordinates, reference angles as $\psi_k^{\text{ref}} = \tan^{-1}((y_{k+1}^{\text{ref}} - y_k^{\text{ref}})/(x_{k+1}^{\text{ref}} - x_k^{\text{ref}}))$ can be computed, and finally δ_k^{ref} can be calculated from (4) by invoking another $\tan^{-1}(\cdot)$. This quickly incurs jaggedness in the δ^{ref}-trajectory and it is ultimately the reason why the solution with $(R,\lambda) = (5,0.7)$ performed worst. While designed to precisely meet steering rate constraints (Fig. 5), after being linked with the straight sections and the use of aforementioned interpolations, steering rate limits are regularly violated by δ^{ref}. Figures 5 and 13(b) should be compared for the case $(R,\lambda) = (8,0)$ and the corresponding differences in steering rate references. Ultimately, while circle-segment smoothing is guaranteed to always violate the δ^{ref}-rate constraint, it does so only for a very short period of time, which is favourable.

5.2. Three characteristic turns

Three characteristic turn manoeuvres that are of special interest in agricultural practice are the U-turn, the Omega-turn and the SGA-turn. The U-turn simulation is visualised in Fig. 14. As motivated by Sabelhaus et al. (2013), if feasible, e.g., enabled by *row-skipping*, the U-turn is the preferred choice for minimisation of total route length. The Omega-turn reference trajectory is given in Fig. 9(b). The SGA-turn is illustrated in Fig. 6(b), where the section from shortly before point S to after

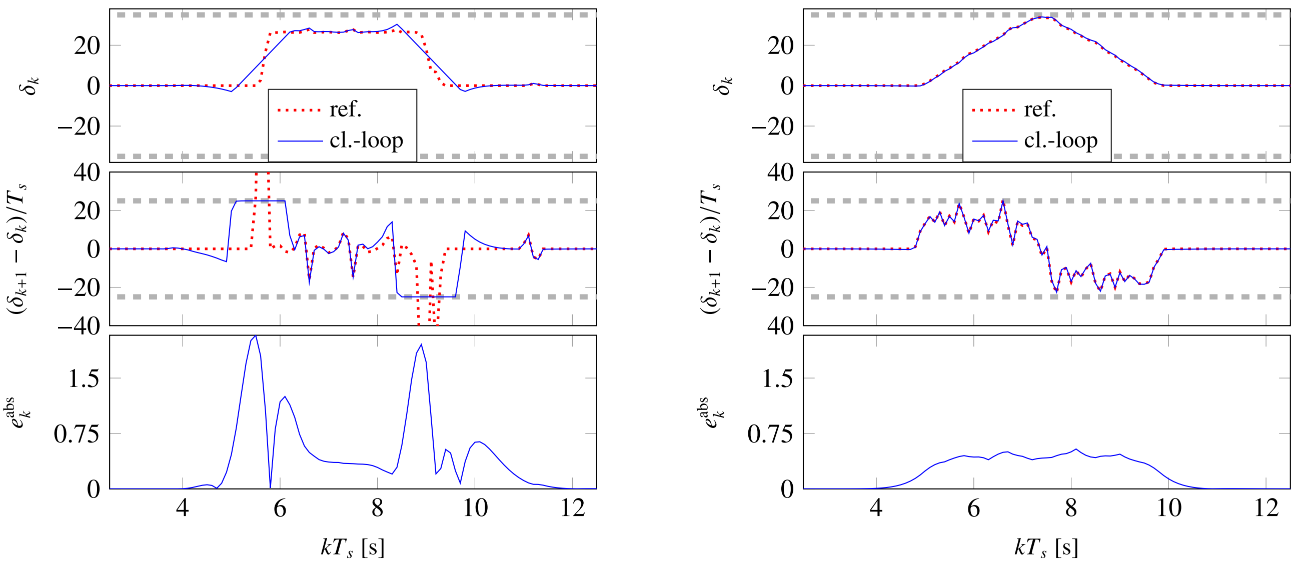

(a) Circle-segment based 90°-transition with $(R, \lambda) = (6, 0.99)$. (b) Clothoid-segment based 90°-transition with $(R, \lambda) = (8, 0)$.

Fig. 13 – Closed-loop tracking results. Note the correlation between tracking error and rate constraint violation. The constraint limits are indicated by the dashed grey horizontal lines.

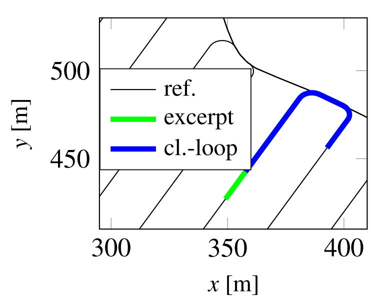

Fig. 14 – Illustration of a typical U-turn manoeuvre. We display the smoothed reference trajectory, an excerpt thereof and the corresponding closed-loop trajectory using LTV-MPC for reference tracking.

Table 4 – Nominal closed-loop simulation results for three experiments, see Section 5.2. For the U-turn, we compare a circle- and clothoid-based version (v1 and v2) with parameters $(R,\lambda) = (6,0.99)$ and $(R,\lambda) = (8,0)$, respectively.

Experiment	$\bar{\tau}_{\mathrm{build}}$	$\bar{\tau}_{\mathrm{q}}/\bar{\tau}_{\mathrm{g}}/\bar{\tau}_{\mathrm{a}}$	$\tau_{\mathrm{q}}^{\max}/\tau_{\mathrm{g}}^{\max}/\tau_{\mathrm{a}}^{\max}$	$\max\{e_k^{\mathrm{abs}}\}$
U-turn (v1)	2.1	6.1/1.5/0.8	9.0/3.0/2.3	2.2
U-turn (v2)	2.1	6.6/1.4/0.8	8.6/2.2/2.1	0.8
Omega-turn	2.1	6.6/1.6/1.0	8.5/2.8/2.1	1.8
SGA-turn	2.1	6.5/1.5/0.8	9.0/2.9/2.2	2.2

P is simulated. Results are summarised in Table 4 and Fig. 14. They are in line with descriptions of Section 5.1.

6. Conclusion

For complicated non-convexly shaped field contours there exists a trade-off between repressed area minimisation and spraying gap avoidance upon which the farm manager must decide. Steering rate constraints and robustness with respect to interpolations must be the driving factors for the reference trajectory design. Circle- and clothoid-segment based path trajectory smoothing have contradicting benefits and disadvantages, respectively. Circle-segments better minimise repressed area and allow for a smaller nominal turning radius with respect to steering angle constraints. However, their resulting reference trajectories always incur a steering rate constraint violation for at least two sampling times. They also provide a maximal absolute tracking error of approximately 2.2 cm in nominal closed-loop simulations. In contrast, purely clothoid-based trajectory design for standard U-turns indicated an accuracy in the mm-range. This was due to references already satisfying steering rate constraints. However, purely clothoid-based segments cause more repressed area and have a larger nominal turning radius that is necessary for the satisfaction of absolute steering angle constraint.

LTV-MPC is a computationally attractive and suitable control strategy for high-precision tracking of previously determined reference path trajectories that were designed under the consideration of system constraints and field geometry. Particularly suited for an embedded application of LTV-MPC seems to be a QP-solver based on ADMM. We consider repressed area minimisation more important than a reduction of maximum absolute tracking error from 2.2 cm to the mm-range under nominal conditions. Therefore, we recommend preliminary edge-smoothing via *circle-segments*. For the generation of SGA- and Omega-turns, we propose to use a combination of circle-segments and bi-elementary paths.

Finally, observing that under constraint-satisfying references mm-tracking precision is achieved, a practical three-step procedure is proposed: a) following above guidelines, generate a first reference trajectory, b) track this first reference in simulation using LTV-MPC under nominal conditions and store the solution as the *second* reference which is now by definition satisfying all constraints, c) use this *second* reference trajectory online for the agricultural machine. This procedure combines efficiently repressed area minimisation while simultaneously offering feasibility for the reference trajectory path.

REFERENCES

Backman, J., Oksanen, T., & Visala, A. (2012a). Navigation system for agricultural machines: Nonlinear model predictive path tracking. *Computers and Electronics in Agriculture, 82*, 32–43.

Backman, J., Oksanen, T., & Visala, A. (2012b). Path generation method with steering rate constraint. In *Proc. International conference on precision agriculture (ICPA)*. Indianapolis: USA.

Backman, J., Oksanen, T., & Visala, A. (2013). Applicability of the ISO 11783 network in a distributed combined guidance system for agricultural machines. *Biosystems Engineering, 114*, 306–317.

Backman, J., Piirainen, P., & Oksanen, T. (2015). Smooth turning path generation for agricultural vehicles in headlands. *Biosystems Engineering, 139*, 76–86.

Bochtis, D., & Vougioukas, S. (2008). Minimising the non-working distance travelled by machines operating in a headland field pattern. *Biosystems Engineering, 101*, 1–12.

Boyd, S., Parikh, N., Chu, E., Peleato, B., & Eckstein, J. (2011). Distributed optimization and statistical learning via the alternating direction method of multipliers. *Foundations and Trends® in Machine Learning, 3*, 1–122.

Dubins, L. E. (1957). On curves of minimal length with a constraint on average curvature, and with prescribed initial and terminal positions and tangents. *American Journal of Mathematics, 79*, 497–516.

Falcone, P., Borrelli, F., Tseng, H. E., Asgari, J., & Hrovat, D. (2008). Linear time-varying model predictive control and its application to active steering systems: Stability analysis and experimental validation. *International Journal of Robust and Nonlinear Control, 18*, 862–875.

Fraichard, T., & Scheuer, A. (2004). From Reeds and Shepp's to continuous-curvature paths. *IEEE Transactions on Robotics, 20*, 1025–1035.

Franke, R. (1998). *Omuses, a tool for the optimization of multistage systems and hqp, a solver for sparse nonlinear optimization*. Technischer Bericht. Deutschland: Institut für Automatisierungs-und Systemtechnik, Technische Universität Ilmenau.

Funke, J., & Gerdes, J. C. (2016). Simple clothoid lane change trajectories for automated vehicles incorporating friction constraints. *Journal of Dynamic Systems, Measurement, and Control, 138*. http://dx.doi.org/10.1115/1.4032033, 021002–021002–9.

Gao, Y., Gray, A., Frasch, J. V., Lin, T., Tseng, E., Hedrick, J. K., et al. (2012). Spatial predictive control for agile semi-autonomous ground vehicles. In *Proc. International symposium on advanced vehicle control (AVEC)*. Seoul: Republic of Korea.

Graf Plessen, M., & Bemporad, A. (2016). Shortest path computations under trajectory constraints for ground vehicles within agricultural fields. In *Proc. IEEE Conference on Intelligent Transportation Systems (ITSC). Brazil: Rio de Janeiro* (pp. 1733–1738).

Graf Plessen, M., Bernardini, D., Esen, H., & Bemporad, A. (2016). Spatial-based predictive control and geometric corridor planning for adaptive cruise control coupled with obstacle avoidance. In *IEEE Transactions on Control Systems Technology* (In revision).

Houska, B., Ferreau, H. J., & Diehl, M. (2011). Acado toolkit–an open-source framework for automatic control and dynamic optimization. *Optimal Control Applications and Methods, 32*, 298–312.

Kanayama, Y. J., & Hartman, B. I. (1997). Smooth local-path planning for autonomous vehicles1. *The International Journal of Robotics Research, 16*, 263–284.

Kayacan, E., Kayacan, E., Ramon, H., & Saeys, W. (2015a). Learning in centralized nonlinear model predictive control: Application to an autonomous tractor-trailer system. *IEEE Transactions on Control Systems Technology, 23*, 197–205.

Kayacan, E., Kayacan, E., Ramon, H., & Saeys, W. (2015b). Towards agrobots: Identification of the yaw dynamics and trajectory tracking of an autonomous tractor. *Computers and Electronics in Agriculture, 115*, 78–87.

Kraus, T., Ferreau, H. J., Kayacan, E., Ramon, H., De Baerdemaeker, J., Diehl, M., et al. (2013). Moving horizon estimation and nonlinear model predictive control for autonomous agricultural vehicles. *Computers and Electronics in Agriculture, 98*, 25–33.

Lenain, R., Thuilot, B., Cariou, C., & Martinet, P. (2005). Model predictive control for vehicle guidance in presence of sliding: Application to farm vehicles path tracking. In *Proc. IEEE international conference on robotics and automation (ICRA)* (pp. 885–890). Spain: Barcelona.

Lenain, R., Thuilot, B., Cariou, C., & Martinet, P. (2006). High accuracy path tracking for vehicles in presence of sliding: Application to farm vehicle automatic guidance for agricultural tasks. *Autonomous Robots, 21*, 79–97.

Leng, Z., & Minor, M. (2010). A simple tractor-trailer backing control law for path following. In *Proc. IEEE/RSJ international conference on intelligent robots and systems (IROS)* (pp. 5538–5542). Taiwan: Taipei.

Oksanen, J., Timo, & Backman. (2015). *Standardization proposal on implement guidance for ISO 11783 compatible tractor-implement systems*, ISBN 978-952-60-6165-8. https://aaltodoc.aalto.fi/handle/123456789/15761.

Oksanen, T., & Visala, A. (2004). Optimal control of tractor-trailer system in headlands. In *Proc. ASAE conference on automation technology for off-road equipment (ATOE)* (pp. 255–263). Japan: Kyoto.

Patrinos, P., & Bemporad, A. (2014). An accelerated dual gradient-projection algorithm for embedded linear model predictive control. *IEEE Transactions on Automatic Control, 59*, 18–33.

Rajamani, R. (2011). Vehicle dynamics and control. In *Mechanical engineering series*. Springer US.

Reeds, J., & Shepp, L. (1990). Optimal paths for a car that goes both forwards and backwards. *Pacific Journal of Mathematics, 145*, 367–393.

Sabelhaus, D., Röben, F., zu Helligen, L. P. M., & Lammers, P. S. (2013). Using continuous-curvature paths to generate feasible headland turn manoeuvres. *Biosystems Engineering, 116*, 399–409.

Scheuer, A., & Fraichard, T. (1996). Planning continuous-curvature paths for car-like robots. In *Proc. IEEE/RSJ international conference on intelligent robots and systems (IROS)* (pp. 1304–1311). Japan: Osaka.

Sharda, A., Fulton, J. P., McDonald, T. P., & Brodbeck, C. J. (2011). Real-time nozzle flow uniformity when using automatic section control on agricultural sprayers. *Computers and Electronics in Agriculture, 79*, 169–179.

Sørensen, C., Fountas, S., Nash, E., Pesonen, L., Bochtis, D., Pedersen, S. M., et al. (2010). Conceptual model of a future farm management information system. *Computers and Electronics in Agriculture, 72*, 37–47.

Thuilot, B., Cariou, C., Martinet, P., & Berducat, M. (2002). Automatic guidance of a farm tractor relying on a single CP-DGPS. *Autonomous Robots, 13*, 53–71.

Van Loan, C. F. (1978). Computing integrals involving the matrix exponential. *IEEE Transactions on Automatic Control, 23*, 395–404.